ORIGINAL PAPER

Time-dependent model for sand grain deflection including contact maturing under sustained load

Dowon Park[1] · Radoslaw L. Michalowski[2]

Abstract
The hypothesis of *contact maturing* advocates static fatigue at contacts between sand grains as the key cause contributing to time effects in sand. The focus of the paper is on a model of an individual grain subjected to a sustained load applied through two steel plates. The grain is characterized by the roughness of its surface. The distinct element method is used to construct a model on two scales: the grain scale and the contact scale. Assemblies of bonded sub-particles are used to model both the grain and the contact region. The bond model includes the stress corrosion process, which simulates decaying strength of bonds and fracture. Two components of the time-dependent grain deflection under sustained loads are the displacement owed to sub-critical fracturing of asperities on the grain surface at the contacts and the creep of the core mineral in the grain. The model demonstrates what may be difficult capturing in physical testing. The simulated nominal contact evolves as the number of contact points increases due to sub-critical fracturing of asperities, leaving the contact firmer. The contact evolution process, as observed in simulations, is consistent with the contact maturing hypothesis.

Keywords Silica sand · Grain-scale behavior · Roughness · Surface topography · Static fatigue · Contact maturing · Subcritical asperity fracture

1 Introduction

Silica sand has a tendency to change some of its properties over time, particularly after a disturbance caused, for example, by deposition, liquefaction or vibratory compaction. The phenomenon, often referred to as *sand ageing* has been known for decades (*e.g.*, [25, 29, 40]), but a definitive explanation for its cause has not been found, Mitchell [30]. Subcritical fracturing of grains has been proposed as a possible cause of the time-dependent behavior of silica sand by Lade and Karimpour [21] and Brzesowsky et al. [5], while static fatigue at contacts between grains has been linked to the time-dependent change in the macroscopic stiffness of ageing sand, Michalowski and Nadukuru [26]. Considerable effort devoted to the mechanical behavior of individual sand

grains can be indicated in the literature [7, 10, 24, 39, 43], though few studies focused on time-dependent behavior of grains and contacts.

Recent experimental evidence suggests that the time-dependent behavior of inter-granular contacts may play a larger role in *sand ageing* than previously thought. Grain-scale experiments on silica sand grains with different roughness indicate that a substantial component of grain deflection comes from the static fatigue process at the contacts, Michalowski et al. [27, 28]. The process, referred to also as *contact maturing*, leads to an increase in the contact stiffness over time. The time-dependent behavior of individual grains and contacts propagates through the spatial scales to influence the macroscopic behavior of grain assemblies and sand deposits. This process can be very consequential in engineering, because an increase in stiffness in confined deposits can lead to an increase in some stress components. Granular geomaterials are pressure-dependent, thus an increase in the first invariant of the stress tensor allows for an increase in shear resistance.

Description of roughness of solid surfaces has been considered for decades, for example, in the early contributions of Archard [2] or Greenwood & Williamson [11]. More

✉ Radoslaw L. Michalowski
   rlmich@umich.edu

1 Department of Civil and Environmental Engineering, University of Michigan, Ann Arbor, MI 48109-2125, USA

2 Department of Civil and Environmental Engineering, University of Michigan, 2028 G.G. Brown Bldg., Ann Arbor, MI 48109-2125, USA

recent contributions involve numerical approaches such as the finite element method, Hyun et al. [17], or the distinct element method, Jerier & Molinari [19]. Time-dependent response of loaded contacts has been a focus of research to a lesser extent, but key experimental results are now available on the nano scale, Li et al. [22], and the micro scale for silica sand grain contacts, Michalowski et al. [27], to provide some guidance for modeling time effects. This paper focuses on modeling of a single grain subjected to sustained loads. Because the total time-dependent deflection of grains is a sum of the displacement owed to creep deformation of the grain core material and the displacement owed to static fatigue at the contacts, the analysis involves two spatial scales, and the model includes two components. The model is to reproduce the grain-scale laboratory tests as well as demonstrate a possible evolution of the nominal contact area during the contact maturing process.

2 Deflection of grains and model overview

This section reports on recent tests for the time-dependent response of individual silica sand grains to sustained loads, crushing, and on the tools used in the modeling effort. The model to be developed in the subsequent section is to mimic the outcome of the physical tests.

2.1 Time-dependent deflection of individual grains

Measuring deflection of grains has been a subject of research primarily in the context of immediate grain response to loads and crushing, and the shear behavior of contacts [6, 8]. Time-dependent grain effects that contribute to the behavior of sand have been studied to a lesser extent. An apparatus for testing time-dependent deflection of grains was described in Wang and Michalowski [46], and the time-dependent grain deflection under sustained diametric loads was reported in Michalowski et al. [27].

Presented in Fig. 1 are the time-dependent deflection curves (convergence of loading plates) for grains subjected to a sustained load of 1.3 and 2.4 N for 25 days, adopted from [27]. The grains had various roughness with the root mean square of the surface elevation (RMS) spanning from 28.6 to 621 nm. These are reported in Table 1. All grains were silica sand grains with a size between 0.65 and 0.80 mm, and the steel loading platens had the roughness of 7.42 nm as defined by RMS. The convergence of the loading platens was found to be very much dependent on the grain surface roughness. The largest convergence after 25 days was for the grain with the largest roughness (RMS = 621 nm), whereas the grains with the lowest roughness (RMS = 26.8 nm)
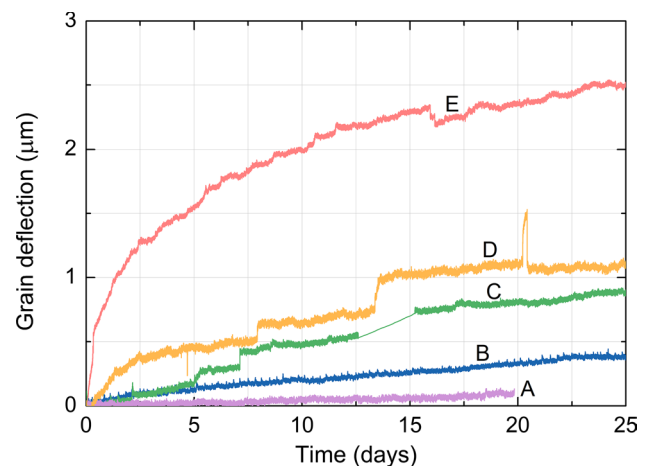
Fig. 1 Deflection of individual grains as functions of loading duration in the grain-scale laboratory testing (data from Michalowski et al. [27]); see Table 1 for details (color figure online)

Table 1 Summary of grain scale tests (after Michalowski et al., 2018)

Test	RMS (nm)	Applied Force (N)	Time-dependent convergence		
			1 day (nm)	5 days (nm)	20 days (nm)
A	28.6	1.3	5	10	100
B	28.6	2.4	10	100	310
C	321	2.4	25	210	780
D	577	1.3	170	451	1090
E	621	2.4	845	1582	2385

exhibited a rather small but steady, approximately constant rate of convergence.

The assumption made in Michalowski et al. [27] suggested that the total convergence is a sum of the displacement caused by the static fatigue of the asperities at the contacts (contact maturing) and the creep of the core material of grains. This conjecture was confirmed by a 6-day test on a very smooth borosilicate glass grain (80% SiO_2) with RMS = 6.28 nm. Under a force of 2.4 N, this test showed a constant convergence coinciding with that of Test B. This rate of convergence is small, and likely due to creep of the core material of the grain, with minimal contribution from static fatigue of the surface asperities. On the contrary, the grain with the largest roughness initially indicates a very large rate of deflection (or convergence of loading plates), likely because of fracturing of asperities, but the process has a decaying characteristic, with the rate of deflection dropping in time to reach approximately the rate consistent with the low-roughness grain creep (Fig. 1).

2.2 Model overview

The model is to mimic the behavior of individual silica sand grains under sustained loads. Because the source of the grain deflection comes from processes at different spatial scales, the model will have two components. The first one will define the time-dependent response of the core material of the grain to the sustained load (creep), and the second one will describe the time-dependent response of the contacts due to contact maturing (static fatigue). The total grain deflection is the sum of the two. Such an approach was suggested earlier in Wang and Michalowski [45] to demonstrate the evolution of the contact region between two grains. The two components of the model are illustrated in Fig. 2, with half of the grain to be simulated to account for the creep of the grain core material (Fig. 2a), and one contact of the grain with a steel plate (Fig. 2c) to be modeled to account for the static fatigue at the contacts. The sum of the two is expected to yield half of the grain deflection.

Both components of the model will involve the distinct element method. The first one includes a half-grain model built of bonded sub-particles to describe the grain core material, and the second one comprises a small disk simulating the contact region. The disk will have a rough surface with textural features susceptible to sub-critical (delayed) fracturing. Both components define material creep, but the term *creep* is a phenomenological category, and it does not reveal the physical mechanism causing the time-dependent effect. The model recognizes that a primary mechanism of time-dependent effects in geomaterials is delayed or subcritical fracturing [41, 42], and it takes advantage of the distinct element method to describe static fatigue through delayed fracturing of inter-particle bonds.

The small contact region subjected to static fatigue, Fig. 2c, is part of the grain, but it is simulated separately because of a much higher resolution of the model needed at the contact scale, compared to the entire grain. The size of the contact disk and the stress boundary conditions will be defined based on a solution of the stress field and deformation in an elastic sphere subjected to a diametric force load, as illustrated schematically in Fig. 2b.

2.3 Distinct element modeling of individual grains and contacts

A typical application of the distinct element method in granular materials involves simulating individual grains as separate (distinct) elements. Here, however, we simulate individual grains as assemblies of bonded sub-particles. The same approach will be used to model contact regions. The bonds have the ability to transfer normal and shear forces from particle to particle as well as the moments, including the torsional moment, Potyondy and Cundall

(a)

(b)

Grain

Plate

Grain

Contact

Plate

(c)
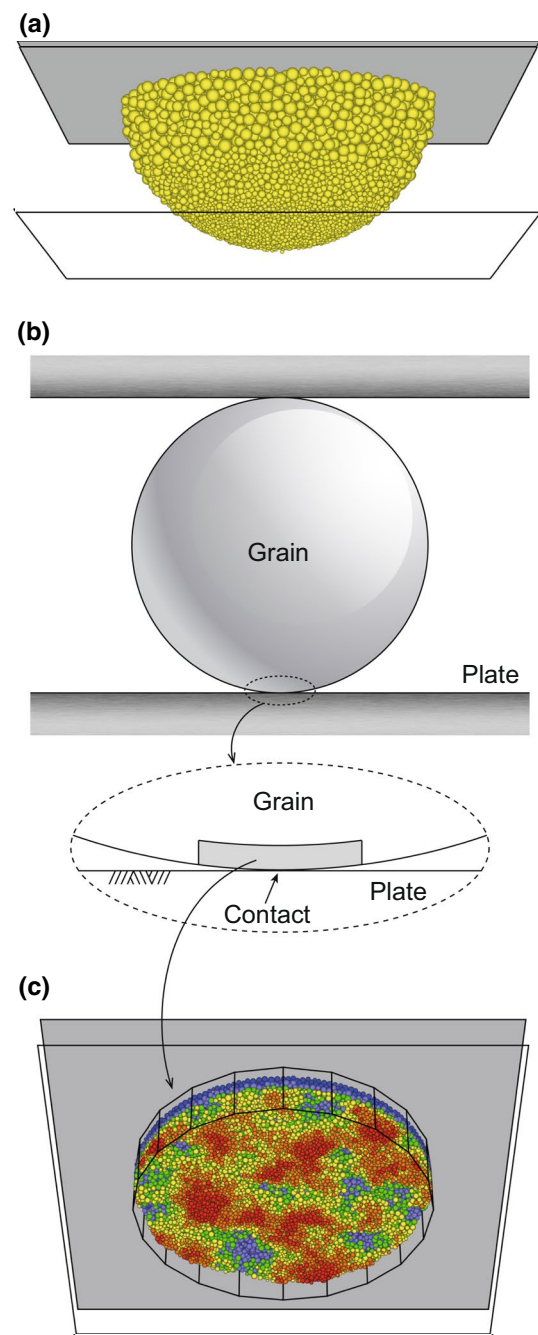
Fig. 2 A schematic for calculating grain convergence: **a** distinct element half–grain model, **b** elastic grain model for estimating the nominal contact size and stresses at the contact region, and **c** distinct element contact model (color figure online)

[37]. Micro-cracking occurs when tensile or shear strength is reached ($\bar{\sigma}_c$ and $\bar{\tau}_c$). The rate effect is introduced into the model through the stress corrosion process of the bonds, Potyondy [38]. Bonds between the spherical sub-particles have diameter $\bar{D}$. When subjected to tension produced by forces or moments, the bond undergoes fatigue modeled

as a reduction in the bond size with the rate of reduction suggested by Potyondy [38] as.

$$\frac{d\bar{D}}{dt} = \begin{cases} 0, & \bar{\sigma} < \bar{\sigma}_a \\ -\beta_1 e^{\beta_2(\bar{\sigma}/\bar{\sigma}_c)}, & \bar{\sigma}_a \leq \bar{\sigma} < \bar{\sigma}_c \\ -\infty, & \bar{\sigma} \geq \bar{\sigma}_c \end{cases} \tag{1}$$

where $\bar{D}$ is the diameter of the bond, β_1, β_2 are the model constants, $\bar{\sigma}_a$ is the activation stress, and $\bar{\sigma}_c$ is the tensile strength.
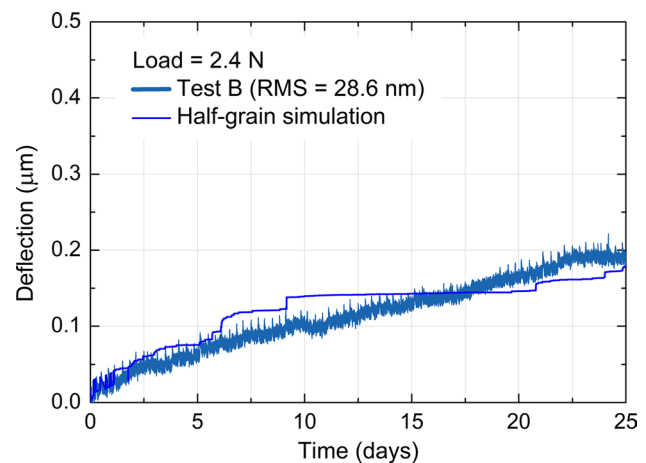
3 Model of the grain core

The physical process responsible for creep of the grain mineral is micro fracturing, Scholz [42], and it is simulated by time-dependent fracturing of bonds between the sub-particles comprising the grain model. Half of the grain is modeled, Fig. 2a, with velocities of the loading plates controlled by a numerical servo-mechanism to maintain a required load on the grain. The size of the specific grain simulated was 800 μm in diameter, with 13,080 spherical bonded sub-particles comprising the half-grain. The size of sub-particles was varied from about 16 μm at the middle of the grain to about 6 μm in the neighborhood of the contact with the bottom plate, where the gradients of stresses are expected to be the largest. The average size of all sub-particles was 9.95 μm. The assembly was modeled using a linear contact law (as implemented in *PFC 3D* code); the same law will be used later in the model of the nominal contact, though on a lower spatial scale. The spherically capped features on the exterior of the half-grain model in Fig. 2a are not spherical surface asperities as in Greenwood and Williamson [11]; they rather represent the constituents of the grain core material. The surface texture is modeled by higher-resolution elements in the contact disk illustrated in Fig. 2c.

This model is expected to yield half of the full grain deflection owed to creep of the core mineral. The physical process driving creep deformation is the subcritical (time-dependent) fracturing of bonds between the sub-particles building the core of the grain. The same physical process will be used to describe contact fatigue (or contact maturing), but the resolution of the model will be finer to mimic the complexity of the surface texture (Sect. 4.3). The model needs two sets of parameters: the bonded particle model parameters, specified in [37], and the stress corrosion parameters, as in [38], governing the time-dependent reduction in bond size defined in Eq. (1).

The bonded particle model was used to look into sand grain behavior by Cil and Alshibli [7], who calibrated it with physical test results. The parameters for the bonded particle model used in our study are listed in Table 2, which includes the calibrated parameters from [7]. In order

Table 2 Properties used in half-grain DEM simulation

Model	Properties	Value
Half-grain	Radius (mm)	0.4
Sub-particle assembly	Mass density, ρ (kg/m³)	2650
	Young's modulus, E (GPa)	70
	Average radius, R_{avg} (μm)	9.95
	Friction coefficient	0.5
	Normal/Shear stiffness ratio, k^n/k^s	2.5
Bonds	Bond radius multiplier, λ	1
	Young's modulus, $\bar{E}_c$ (GPa)	70
	Normal/Shear stiffness ratio, $\bar{k}^n/\bar{k}^s$	2.5
	Mean normal strength, $\bar{\sigma}_c$ (MPa)	750
	Mean shear strength, $\bar{\tau}_c$ (MPa)	750
	Standard deviation of normal and shear strength (MPa)	175

Fig. 3 Half-grain DEM calibration with Test B measurements

to determine the parameters for the static fatigue (stress corrosion process) in the core material of the grain, the model was calibrated with the experimental results from a test with the smallest roughness among the test results available. The deflection of the grain in Test B (Fig. 1) is expected to be owed predominantly to stress corrosion micro-cracking inside the core material of the grain; the very low roughness (RMS = 28.6 nm) makes the grain surface resistant to contact fatigue caused by fracturing of surface asperities at the contact. A series of simulations was then carried out, with various combinations of model parameters, to match the outcome with Test B convergence. The outcome of this calibration effort is shown in Fig. 3; simulated half-grain deflection was matched to half of the Test B deflection after 25 days under the load of 2.4 N. Calibrated parameters β_1, β_2 and $\bar{\sigma}_a$ in the stress corrosion process, Eq. (1), are listed in Table 3.

Table 3 Stress corrosion model parameters calibrated on Test B

| Property	Value
β_1 (m/s)	1×10^{-14}
β_2	25
Activation stress, $\bar{\sigma}_a$ (MPa)	50

4 Nominal contact model

The second component of the grain deflection comes from the interaction of the rough surface of the grain with the steel plates at the contacts. The contact surface will be simulated using the distinct element method, but simulation of the roughness requires higher resolution than that used in simulations of the half-grain. For that reason, only the contact region in a form of a disk, with a thickness not exceeding 6 μm, will be modelled. The diameter of the contact disk and the stress boundary conditions will be determined from finite element simulations of an elastic sphere (grain) in contact with steel loading plates.

4.1 Grain elastic model

The finite element model of the elastic sphere is shown in Fig. 4a. The model is axi-symmetric and only half of its diametric cross-section was modelled; the view of the sphere was generated by rotating the mesh by 270° about the symmetry axis. Figure 4b indicates the distribution of the radial stresses, σ_{rr} (in the spherical coordinate system with the origin in the center of the sphere) and circumferential stresses $\sigma_{\theta\theta}$ are illustrated in Fig. 4c. These stresses will be taken as boundary conditions on the contact disk, shown in the lower part of Fig. 4a, in order to simulate the response of the nominal contact to sustained loads. Circumferential stresses are tensile in an oval (dark) region above the contact with the plate, Fig. 4c.

Calculations were performed using the Abaqus environment. Element type CAX4R was used to build an axisymmetric model. The number of elements in the half sphere cross-section was 1950 and 800 elements in each of the top and bottom plates. The bottom and top plates were loaded with uniformly distributed loads equal to the required forces used in the tests simulated. A more refined element mesh was used in the contact region for better numerical accuracy. The deforming contact region was updated during the loading process to account for geometric nonlinearities. Material properties used in calculations are given in Table 4.
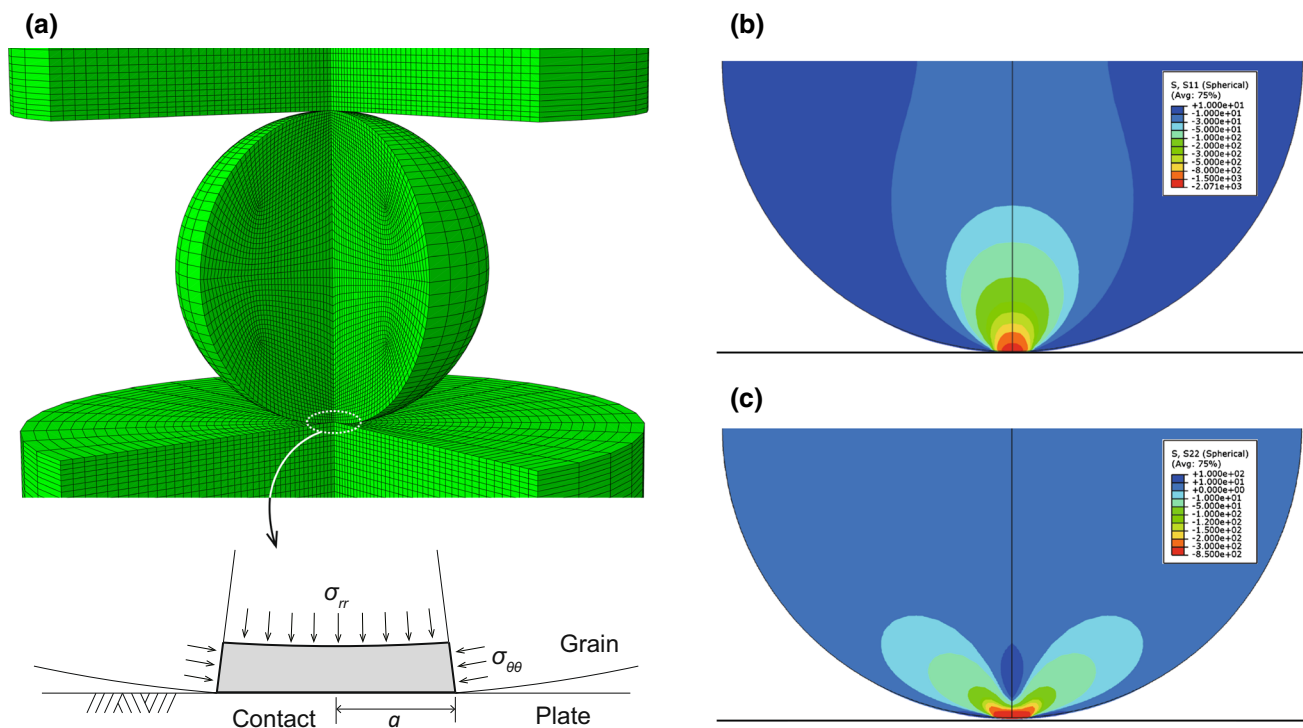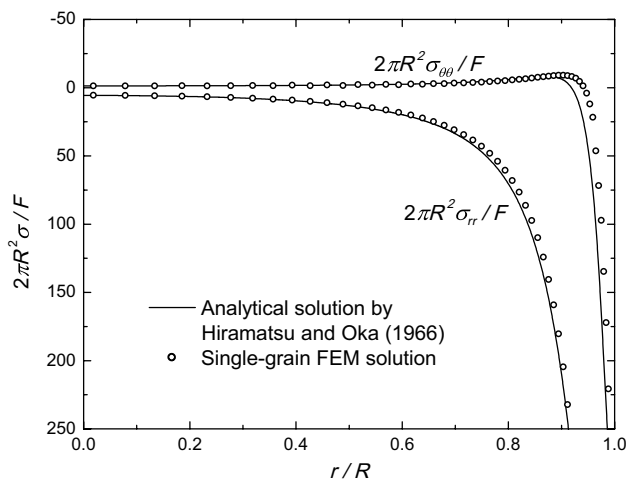
Fig. 4 Axi-symmetric single-grain elastic FE model: **a** geometric configuration and mesh discretization of a sand grain in contact with steel plates, **b** distribution of radial stress σ_{rr}, and **c** distribution of circumferential stress $\sigma_{\theta\theta}$ (color figure online)

Table 4 Physical and mechanical properties used in FEM simulation of grain contact

	Sand	Plate
Elastic modulus, E (GPa)	70	200
Poisson's ratio, v	0.17	0.3
Mass density (kg/m^3)	2650	7700
Friction coefficient	0.5	0.5

Table 5 Stress components and radius of nominal contact from FEM

	F = 1.3 N	F = 2.4 N
σ_{rr} (MPa)	1088	1222
$\sigma_{\theta\theta}$ (MPa)	235	276
Nominal contact radius a (μm)	19.5	25.0

The finite element solution was compared to the analytical solution by Hiramatsu and Oka [15] (see also [16, 34]) and the comparison of the circumferential stress and radial stress along the vertical radius is illustrated in Fig. 5. The small discrepancy is likely caused by the difference in boundary conditions. Hiramatsu and Oka [15] considered the applied load as uniform traction on a small surface region, whereas the traction distribution on the contact region in the finite element model was part of the solution and it was not uniform. Stresses σ_{rr} and $\sigma_{\theta\theta}$ to be used as boundary conditions in the contact disk simulations came from the finite element analysis and are given in Table 5. Stress σ_{rr} was taken as $F/(\pi a^2)$ (F - force on grain, a - contact radius from FEM), whereas stress $\sigma_{\theta\theta}$ was taken at the location of the nominal contact boundary estimated as $r/R = 0.993$ and $\theta = 0.024$ rad (for F = 1.3 N) and $\theta = 0.031$ rad (for F = 2.4 N). Coordinates r/R and θ are taken in the spherical coordinate system with the origin at the center of the spherical grain. Stresses $\sigma_{\theta\theta}$ from the analytical solution, Hiramatsu and Oka [15], were 248.86 MPa and 298.07 MPa, for 1.3 and 2.4 N loads, respectively; the difference between these and those in Table 5 are likely owed to different boundary conditions.

Because of geometric nonlinearities, stresses in the contact region are not proportional to the force applied.

Radius a of the contact area following from the finite element model was compared to one calculated from the Hertz [14] solution for a contact between an elastic sphere and the elastic half-space.

$$a = \left(\frac{3FR}{4E^*} \right)^{\frac{1}{3}} \tag{2}$$

where F is the force and R is the radius of the sphere, and the elastic modulus E^* is calculated from

$$\frac{1}{E^*} = \frac{(1 - v_1^2)}{E_1} + \frac{(1 - v_2^2)}{E_2} \tag{3}$$

where 1 and 2 refer to the Poisson's ratios and Young's moduli of the sphere and the half-space. Hertz's solution yields a radius a of 19.0 μm and 23.3 μm for the load F of 1.3 N and 2.4 N, respectively. The values are slightly lower than those from the finite element analysis in Table 5.

4.2 Numerical generation of surfaces at contacts

The aim in this subsection is to construct a distinct element model of a silica grain surface. A similar approach to modeling contact surfaces using the distinct element method can be found in [19]. Only the contact region of the size determined in the previous subsection will be modelled, allowing mimicking of the roughness of the silica grain surface. The model can only mimic the shape of the contact surface with limited resolution, determined by the size of sub-particles used to construct the model topography. The process includes the following steps (illustrated in Fig. 6 for the surface of the grain used in Test E, Fig. 1):

1. Surfaces of grains to be simulated are scanned in the Atomic Force Microscope (AFM), Fig. 6a,
2. elevation profiles from AFM are processed to obtain statistical information,
3. a rough surface matching the AFM-scanned surface is generated based on idealized Power Spectral Density (PSD), Fig. 6b,
4. a disk-like contact region is constructed of bonded sub-particles; the diameter of the disk is determined from

Fig. 5 Comparison of FEM-calculated dimensionless stresses $2\pi R^2 \sigma_{rr}/F$ and $2\pi R^2 \sigma_{\theta\theta}/F$ with solution of Hiramatsu and Oka (1966) along the vertical normalized radial coordinate r/R (R - sphere radius, F – force, Poisson's ratio 0.17)

Fig. 6 Steps in generation of the surface in the nominal contact model: **a** AFM scan of the grain surface, **b** numerically generated surface to mimic the true surface, **c** high-resolution contact disk, and **d** carved surface of the contact disk (RMS = 621 nm) (color figure online)
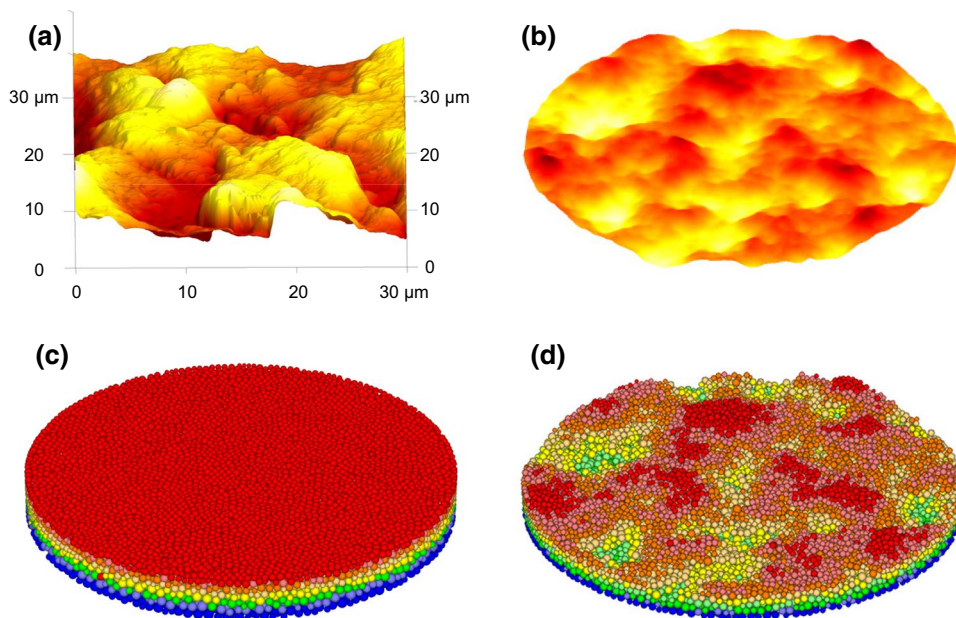
the FEM solution of an elastic spherical grain in contact with a steel loading plate, Fig. 6c,

5. distinct element assembly in Fig. 6c is carved to match the model of the rough surface, Fig. 6d.

Power Spectral Density function (PSD) was employed to characterize the surface of the grain and its statistical roughness [3, 35]. The PSD functions for different grain surfaces were approximated with self-affine surfaces, and were used to recreate the contact surfaces numerically. The AFM scan was not used directly, because of the size mismatch of the 30×30 µm square AFM scan and the circular nominal contact surface of 39 µm and 50 µm in diameter, as needed in simulations with 1.3 and 2.4 N loads. The roughness RMS of the loading plate, Fig. 2c, was determined from the AFM scan as 7.42 nm, and it was not modeled. Modeling of the plate roughness would require a much more refined resolution than that allowed by sub-elements of 360 nm in diameter [19].

The forward discrete Fourier transform of the surface profile $h_{x,y}$ is calculated as

$$\tilde{h}_{q_x,q_y} = l_x l_y \sum_{x,y} h_{x,y} e^{-i(q_x x + q_y y)} \tag{4}$$

where q_x and q_y are wavevectors (spatial frequencies). The discrete elevation information $h_{x,y}$ is given here in a rectangular area of lengths L_x and L_y in the x and y directions, respectively, and with the grid defined by l_x and l_y ($m \times n$ being the number of elements in the grid, $m = L_x/l_x$, $n = L_y/l_y$). The PSD function is defined as the squared amplitude of the forward Fourier Transform (*e.g.*, Jacobs et al. [18]).

$$C^{2D}_{q_x,q_y} = A^{-1} \left| \tilde{h}_{q_x,q_y} \right|^2 \tag{5}$$

where A is the surface area ($A = L_x L_y$) with given topography information. Wavevectors q_x and q_y have upper and lower limits defined by the surface size; the smallest wavelengths are $2\pi/L_x$ and $2\pi/L_y$, whereas the largest wavelengths are $2\pi/l_x$ and $2\pi/l_y$. Observations of surfaces of silica sand grains indicate isotropy of the elevation distribution, Yang et al. [48]. Consequently, PSD can be represented as a function of wavevector q ($q = \sqrt{q_x^2 + q_y^2}$), with PSD denoted as C_q.

Self-affine surfaces were discussed by Archard [2] well before the term *fractal* was coined. He considered surfaces with a system of spherical asperities and each asperity covered with smaller spherical asperities. PSD functions of self-affine surfaces, as those considered by Archard, show a form of $C_q \propto q^{-2-2H}$, where H is the Hurst exponent associated with fractal dimension D_f ($H = 3 - D_f$), [23, 35]. PSD functions for surfaces of grains used in sustained-load experiments (Fig. 1) are shown in Fig. 7a. They are consistent with self-affine PSDs for geomaterials [32, 44, 48]. Idealized PSD functions for the specific grain surfaces were constructed, consistent with

$$C_q = C_0 \, q^{-2-2H} \tag{6}$$

where C_0 is a constant defining the shift of the PSD function. These are fitted between the maximum and minimum wavevectors. Each fit is characterized by a *roll-off* wavevector such that the PSD becomes constant for wavevectors smaller than the roll-off value. The best fit of the idealized
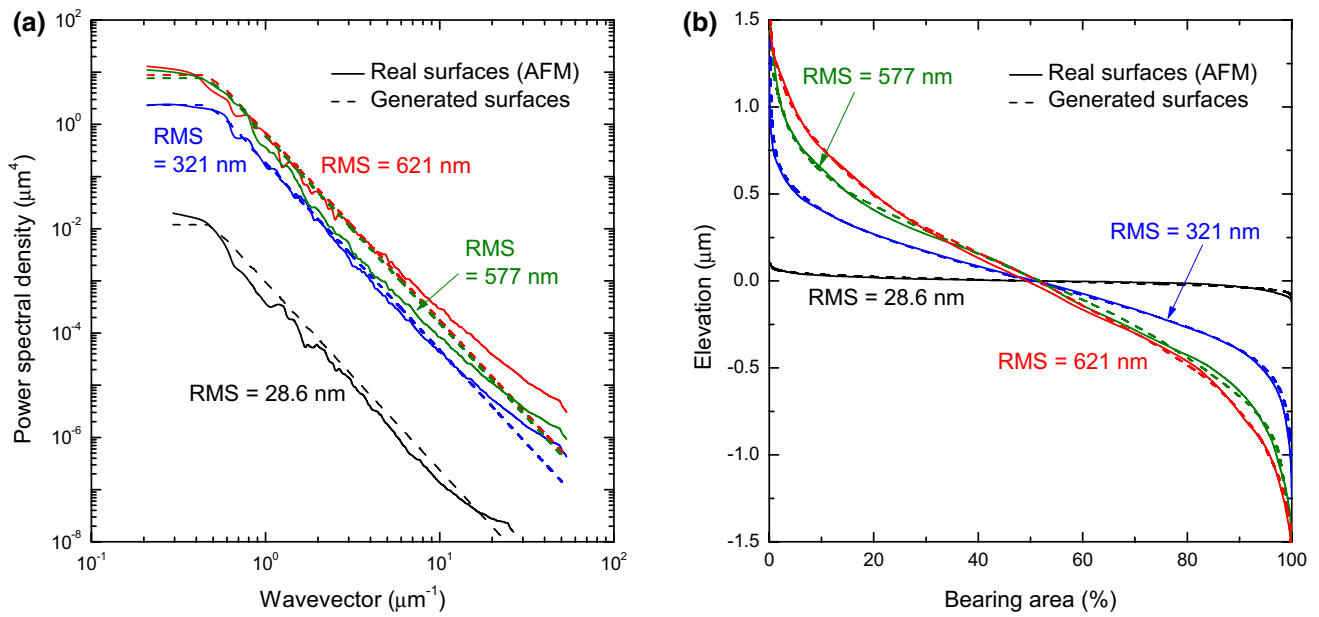
Fig. 7 Statistical measures of sand grain surfaces and numerically generated surfaces: **a** power spectral density (PSD), and **b** bearing area curve (BAC) (color figure online)

PSD into those processed from the AFM measurements of the sand grain surfaces indicates the Hurst exponent H of 0.8 and the roll-off wavevector of 0.5 μm^{-1}. Constant C_0 in Eq. (6) is obtained from Parseval's theorem applied to the Root Mean Square (RMS) of the surface elevation.

$$\mathrm{RMS}^2 = \frac{1}{A} \sum_1^n \sum_1^m \left| C_q \right| \qquad (7)$$

Having determined the PSD for idealized (self-affine) and isotropic surfaces, the amplitude of the Fourier transforms can be obtained by reversing Eq. (5) [18]

$$\left| \tilde{h}_{q_x,q_y} \right| = \sqrt{C^{2D}_{q_x,q_y} A} \qquad (8)$$

Because Eq. (8) only includes the amplitude of wavevectors (a matrix with real numbers), the phase was randomly chosen from the range $[0, 2\pi]$ to yield Fourier transforms $\tilde{h}_{q_x,q_y}$ (complex numbers matrix). The elevation profiles $h_{x,y}$ for the surface to be generated were calculated by the inverse discrete Fourier transforms

$$h_{x,y} = \frac{1}{L_x L_y} \sum_{q_x,q_y} \tilde{h}_{q_x,q_y} e^{i(q_x x + q_y y)} \qquad (9)$$

This random surface generation technique was used earlier by Kanafi and Tuononen [20]. The method allows easily generating rough surfaces of any shape with the statistical characteristics of elevation distribution consistent with the prototype surfaces used in the tests.

An additional surface characterization technique used is Bearing Area Curve (BAC) or the Abbott-Firestone curve. It is a cumulative curve of the distribution histogram of the elevation profile. A point on the plot yields the probability of the elevation being higher than a given elevation. Compared to the histogram, the BAC is less susceptible to discretization of the elevation interval, resulting in a relatively smooth curve [3]. The comparisons of the BAC of real sand grain surfaces to the surfaces generated by PSD are shown in Fig. 7b. Overall, the comparisons show a very good agreement.

4.3 Nominal contact simulation and total convergence results

The nominal contact model has radius a dependent on the load, and determined from simulations of an elastic grain (Table 5). The curvature of the contact disk was not replicated in the model, because of a small contact disk diameter compared to the diameter of the grain. The grain elastic FEM model, Fig. 4, simulates deformable bodies, a sand grain and steel plates, but the grain DEM model, Fig. 2a, considers a rigid plate. The radius of a nominal contact in DEM simulation would underestimate that from the FE model, because of the increased effective elastic modulus in Eq. (3). Also, Greenwood and Tripp [12] indicated that the nominal contact area of a rough surface would be larger than one of a smooth contact. For the time-dependent grain deflection process under constant load considered in the paper, these effects were judged small compared to those associated

with the time-dependent increasing number of contact points within the nominal contact area, Fig. 11. Therefore, they were not directly considered in the simulations.

The nominal contact has a variable thickness between 3 and 6 µm, dependent on the surface profile. Roughness profiles for all grains in Table 1 were contained within an amplitude of less than 3 µm, which was well accommodated in the 6 µm model thickness before carving. This thin disk-like DEM assembly, Fig. 6d, was intended to account for the deflection owed to fracturing and crushing of the surface asperities (contact fatigue or maturing), whereas grain deflection due to deeper layers of the underlying mineral is accounted for by creep of the core material. The latter is modeled as time-delayed (subcritical) fracture of bonds between the sub-particles building the grain. The DEM nominal contact disk was thin enough to exclude the creep of underlying layers (accounted for in the half-grain model), but thick enough to include the lowest valleys after carving and prevent structural failure of the disk during simulations.
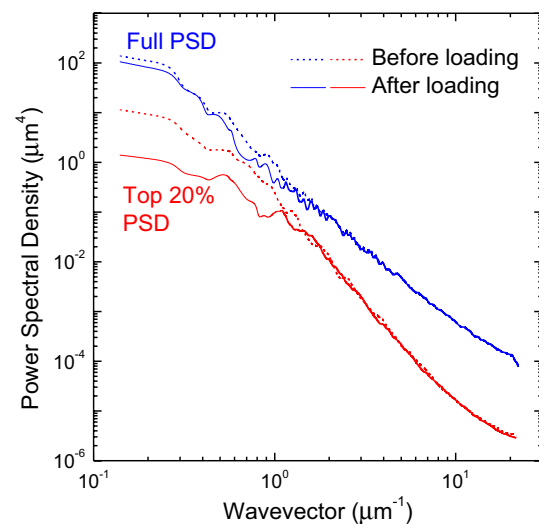
Carving of the model was carried out by superimposing the numerically generated rough surface over the assembly of the sub-particles in the contact disk (Fig. 6c), and deleting all sub-particles outside of the target surface. This model is to describe the deflection due to fracturing of the surface asperities, thus the small thickness. Because of the creep in the grain core material, one might argue that radius a of the nominal contact will increase in time. The true contact, however, is formed between the asperities on the grain and the surface of the plate. An increase in the number of true contact points is accounted for by the model, but the increase in the nominal contact size is ignored, as the influence of the grain material creep on the contact size was judged negligible for the load duration considered. The presence of moisture is known to have an effect on contact behavior. Pressure dissolution of minerals at the tips of asperities accelerates the static fatigue process. For that reason, the physical tests (Fig. 1) were carried out in an environmental chamber under constant relative humidity ($30 \pm 5\%$) and temperature (20 ± 1 °C), expecting a constant influence over time of these environmental factors. Simulations are then considered valid for those conditions.

The roughness of grain surfaces is characterized by complexity of their morphology, which makes it difficult to mimic precisely by a model, which consists of spheres of varied size at the resolution used. Accurate modeling of the texture is also essential to assess the contact stiffness [13, 49]. The emphasis of this paper is on demonstrating a model, which can describe the deflection of a sand grain under sustained loads, and can be calibrated with existing data. Essential to such a model is describing the time-dependent influence of contact fatigue on the grain deflection. Observations of contacts subjected to sustained loads indicate that the fatigue process is more distinct in the upper elevation portion
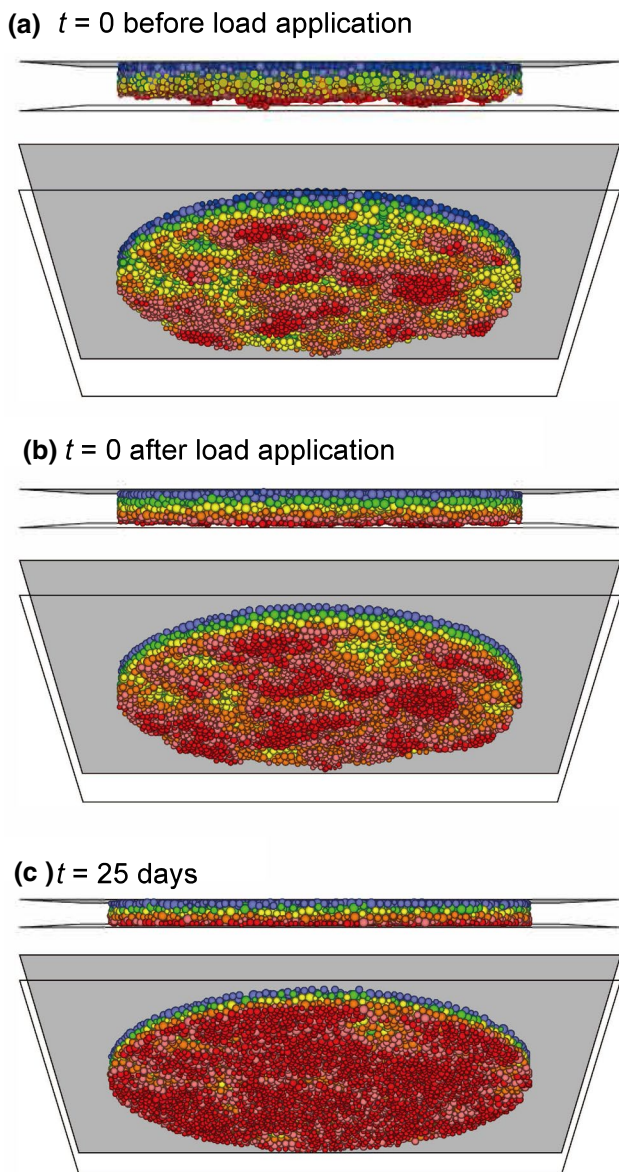
of the morphology. This is confirmed in Fig. 8, where power spectral densities are plotted for a contact region on a silica sand grain subjected to sustained load. The change caused by loading is very distinct when the upper 20% of the elevation spectrum is considered, whereas it is much less discernable when considering the full power spectrum density. Consequently, it may be important to mimic the tall asperities with a high degree of accuracy, but not as important to precisely represent the asperities found in the lower part of the elevation profile. By using the relatively high-resolution model with bonded sub-particles and carving the surface, we mimic the surface accurately in the region where it matters the most. This might need to be modified if the focus is, for example, on evaluation of contact stiffness [13].

A nominal contact model used for the simulations of Test E (Table 1) is illustrated in Fig. 9a. The model included 20,583 bonded sub-particles (8806 after carving), with an average radius of 0.36 µm and the stiffness of contacts between sub-particles as in Table 2. Some sensitivity analysis regarding the size of the sub-particles in the model is included in Sect. 5. The strength of geomaterials, however, exhibits a size effect [4, 31] and the bond strength calibrated for simulating the entire grain is not sufficient for simulations of a disk 6 µm in thickness.

In order to determine the bond strength to be used in the distinct element model of the nominal contact, a calibration effort was carried out. Simulations of the deflection of the nominal contact regions in Tests B, C and E (Table 1) were carried out to match with experimental convergence in the tests (Fig. 1). For each test, the model was carved to match the respective roughness. The calibration simulations
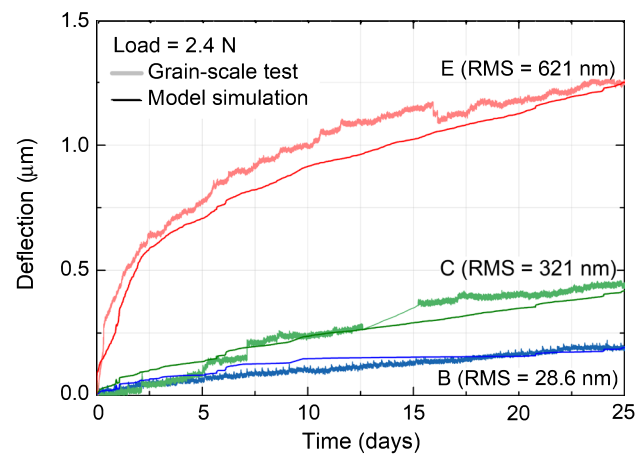

Fig. 8 Evolution of surface morphology represented by Power Spectral Density of the full elevation profile and the upper 20% profile on a silica sand grain contact subjected to sustained loading of 2.4 N for 3 days (color figure online)

(a) *t* = 0 before load application

(b) *t* = 0 after load application

(c) *t* = 25 days

Fig. 9 Distinct element model of the contact region simulating Test E: **a** carved surface, **b** immediately after load application, and **c** after 25–day loading with 2.4 N (color figure online)
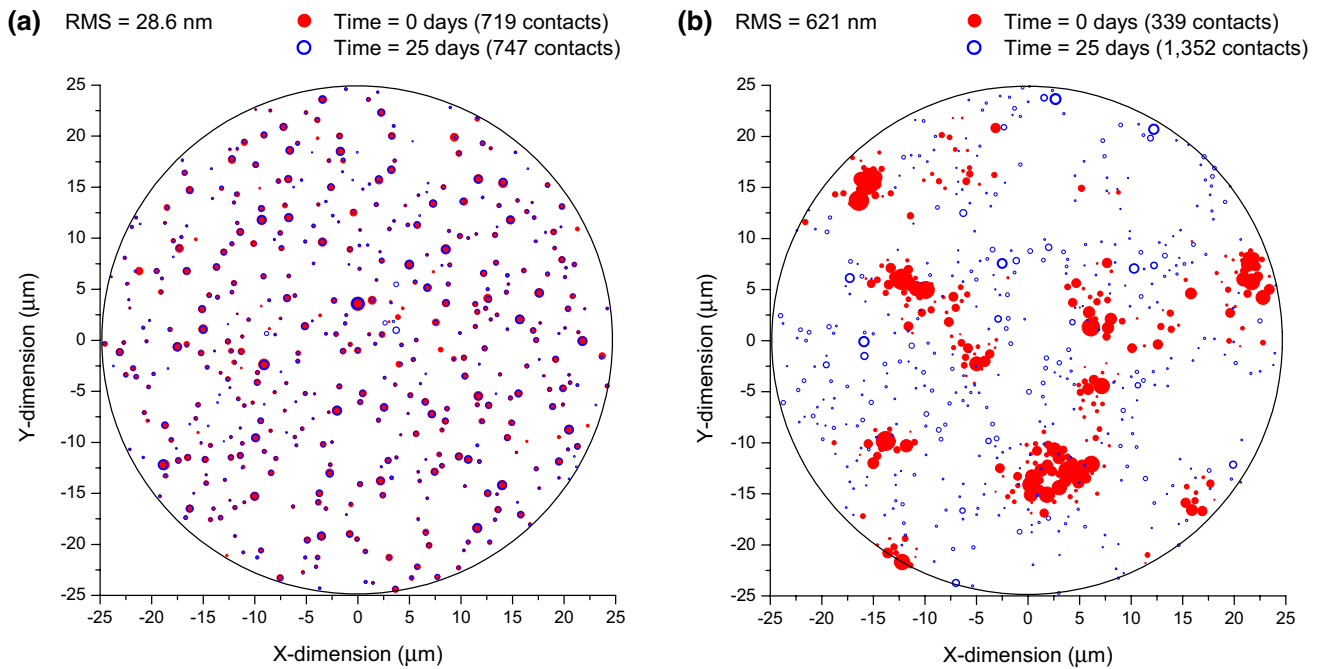
Fig. 10 Experimental grain convergence data (Tests B, C, E) and simulated calibration curves (color figure online)

The side view, immediately after load application, shows a much smoother profile, because of the immediate fracturing of bonds between sub-particles (damage), but the bottom view of the surface still indicates a substantial roughness. In the next 25 days of sustained loading of 2.4 N, the simulated contact topography continues to evolve owing to sub-critical bond fracturing. The contact disk continues to deform, contributing to the total grain deflection. The nominal contact is left with an increased number of contact points between the simulated asperities and the loading plate, and the contact has a visual appearance of a smoother surface, Fig. 9c.

4.4 Contact maturing

Among the three calibration simulations in Fig. 10, tests B and E were selected to observe some of the features of the contact maturing process. The grains in tests B and E are characterized by very different roughness: RMS of 28.6 and 621 nm, respectively. In the case of very low roughness, the bulk of the grain deflection is expected to come from creep of the grain material, whereas for the large roughness, the contact maturing is likely to be the predominant process immediately after load application.

Contact points, force chains propagating through the sub-particles, and bonding breakage in simulations of the nominal contacts were monitored over the duration of 25 days. The distribution of the contact points immediately after the load of 2.4 N was applied is illustrated in Fig. 11a and b by the red-filled circles (bubbles). The larger the bubble, the larger the force at the contact point (the sum of bubble areas remains the same at every instant during the entire simulation, indicating constant force). In the simulation of Test B, the initial number of contact points was 719, and they were fairly uniformly distributed over the entire area of the nominal contact. After 25 days of sustained loading,

are shown in Fig. 10. These curves include the sum of the deflection from simulations of one nominal contact and half of the entire grain (Sect. 3), whereas the experimental curves include half of the total deflection from Fig. 1. Matching of the three pairs of curves in Fig. 10 was reached for the bond strength for both $\bar{\sigma}_c$ and $\bar{\tau}_c$ Maturing of contacts and ageing of silica sand equal to 10 GPa.

A side view and the bottom view of the carved contact disk model used in test E are shown in Fig. 9a. The contact geometry immediately after the load of 2.4 N was applied, is depicted in Fig. 9b. Varied colors of the sub-particles were used only for better visual recognition of the surface shape.

Fig. 11 Contact points and contact forces captured in the nominal contact model: **a** RMS = 28.6 nm, and **b** RMS = 621 nm (color figure online)

the number of contact points (blue circles) increased by a small amount to 747 (less than 4%), retaining approximately uniform spatial distribution. The initial number of contact points in contact with the rough surface (RMS = 621 nm) was 339 (less than half of those for the much smoother surface with RMS = 28.6 nm), and the distribution of them was more concentrated, with large forces transferred through several 'focused' areas. This is expected because of the larger amplitude between the peaks (asperities) and valleys on the contact area. During the 25-day process of loading, the static fatigue process causes the number of contact points to increase dramatically to 1352, a nearly fourfold increase. This increase is thought to be caused by asperity fracturing, modeled as bonding breakage between sub-particles forming the textural features in the surficial layer of the nominal contact model. The force is now transferred through the contact more uniformly, still not as homogenously as in the contact with small roughness.
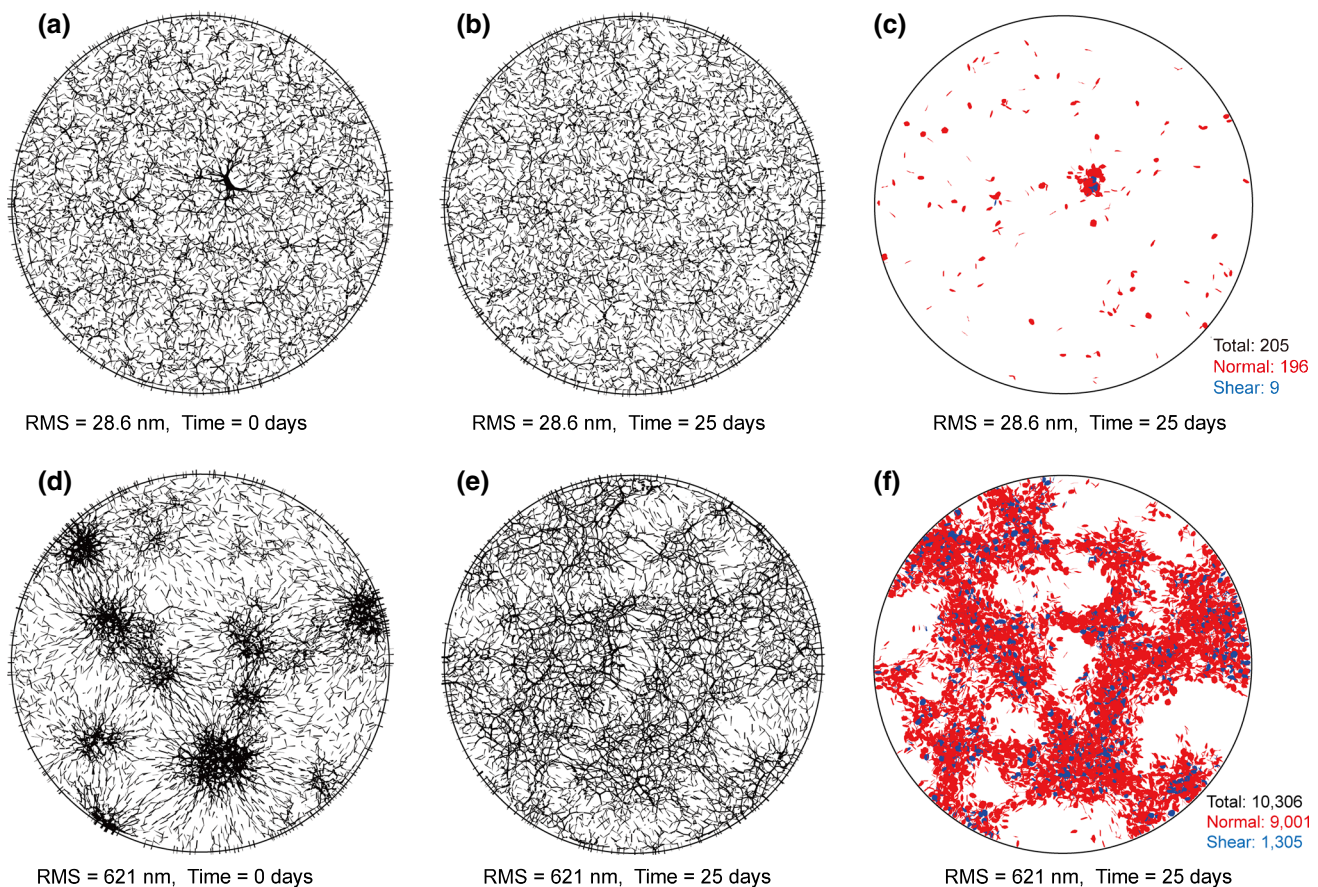
The resolution of the models is defined by the size of the sub-particles used in the construction of the contact. One needs to expect that the number of contact points and its increase during the simulation of the maturing process are dependent on the resolution. Still, the model demonstrates the trends in the contact maturing process consistent with the contact maturing hypothesis [26, 27].

Force chains and time-dependent bonding breakages between sub-particles (simulating fracturing) are shown in Fig. 12. Plots a, b, d and e show projections of force chains in the nominal contact disk on the plane of the contact. The

thickness of the lines in the force chain networks is proportional to the intensity of the force carried by the chain. Images c and f show the projection of bond fractures that occurred in 25 days after the load application. Fractures owed to the stress corrosion process are marked red, whereas bond breakage caused by reaching the bond shear strength are marked blue. The numbers of fractures are marked to the bottom-right in plots c and f. Force chains in the relatively smooth contact (RMS = 28.6 nm), Fig. 12a, are initially almost uniformly distributed, with one small concentration close to the center's upper-right. In 25 days of sustained load, this concentration has "dissipated", Fig. 12b, leaving a small area with concentrated fractures, Fig. 12c. A relatively small number of fractured bonds (205) after 25 days is distributed over the entire contact disk, with the exception of a small area of damage concentrated at the location of the initial force chain concentration.

The rough contact (RMS = 621 nm), Fig. 12d, starts with a substantial concentration of the force chains in several locations, indicating concentrations in intensity of the force transferred through the contact. The Reader will notice a relation of these concentrated force chains and the intensity of the force initially transferred through the contact, illustrated in Fig. 11b. In the subsequent 25 days, Fig. 12e, new contact points were created due to fracturing of simulated asperities, and the force chain network becomes more uniform. The fractures (breakages of bonds between sub-particles), Fig. 12f, are concentrated at locations where, initially, the forces were transferred with high intensity (Fig. 12d),

(a) RMS = 28.6 nm, Time = 0 days

(b) RMS = 28.6 nm, Time = 25 days

(c) RMS = 28.6 nm, Time = 25 days

Total: 205
Normal: 196
Shear: 9

(d) RMS = 621 nm, Time = 0 days

(e) RMS = 621 nm, Time = 25 days

(f) RMS = 621 nm, Time = 25 days

Total: 10,306
Normal: 9,001
Shear: 1,305

Fig. 12 Force chains and micro-cracks (bonding breakage): **a** force chains at $t=0$ (RMS$=28.6$), **b** force chains at $t=25$ days, **c** bonding break-age at $t=25$ days, **d** force chains at $t=0$ (RMS$=621$ nm), **e** force chains at $t=25$ days, and **f** bonding breakage at $t=25$ days (color figure online)

presumably because of elevated asperities. The time-dependent process of bond breaking is much more intense at the contact with high roughness; the total number of fractures is now 10,306 after 25 days of a sustained load of 2.4 N. Fracturing of simulated asperities gives rise to large displacements of grain surface, substantially contributing to the grain deflection.

5 Model assessment

To acquire some indication for the sensitivity of simulations on the resolution of the model, the nominal contact (in Test E) was simulated with different numbers of sub-particles (N) in the carved contact disk, but with the same stiffness and bond strength properties (as calibrated). The outcome of simulations is given in Fig. 13. The differences in the four simulations are produced not just by the different number of sub-particles in the model (varied from 7106 to 14,204), but also by unavoidable variation in the packing in the randomly generated models.

Load = 2.4 N, RMS = 621 nm
— N = 14,204
- - N = 10,206
-·- N = 9,495
-··- N = 8,806
···· N = 7,106
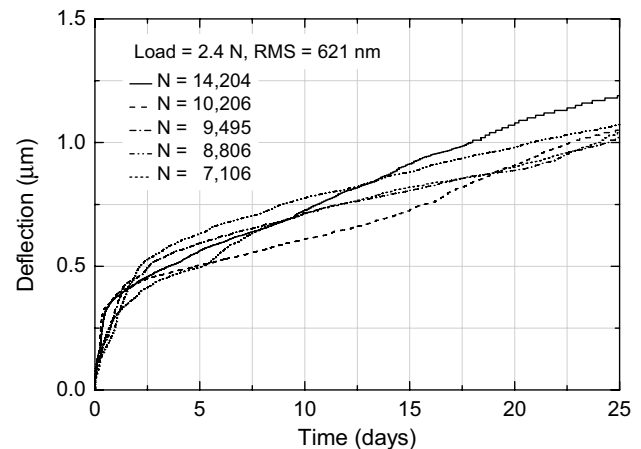
**Fig. 13** The effect of the model resolution on deflection of the nominal contact model

This weak dependency on the element size was also found in another DEM rough surface contact model [19], as well as finite element models [17, 33], the boundary

element method [36], and the combined finite and discrete element method studies [47].

A relatively good agreement of the grain convergence in the laboratory tests and in the model simulations in Fig. 10 is not surprising, because the figure shows the calibration simulations. The model validation requires applying the model with calibrated parameters to predict an outcome in independent tests carried out on grains with different, but known roughness and under different load conditions. Experimental results of time-dependent deflection of grains are scarce, and the only tests known to the authors are those in Table 1. Tests A and D, with sustained load of 1.3 N, were simulated with parameters calibrated on Tests B, C and E (Fig. 10). Because the load is now different from that used in calibration simulations, the contact area and stresses on the contact disk are also different (Table 5).

The respective comparisons are illustrated in Fig. 14. The convergence process of the grain with RMS of 577 nm and load of 1.3 N (Test D) has some discontinuities (steps), likely associated with fracturing of larger asperities. A spike at the 20-day mark, however, is likely due to some irregularity in the power supply. The simulation follows the experimental curve with reasonable accuracy, considering the model mimics the true texture of the contact surface with accuracy limited by the size of the sub-particles used in the distinct element model of the contact. Simulation of Test A, which predominantly includes the convergence due to creep of the core mineral of the grain, appears to overestimate the displacement. The trend, however, appears to be consistent with the test curve.
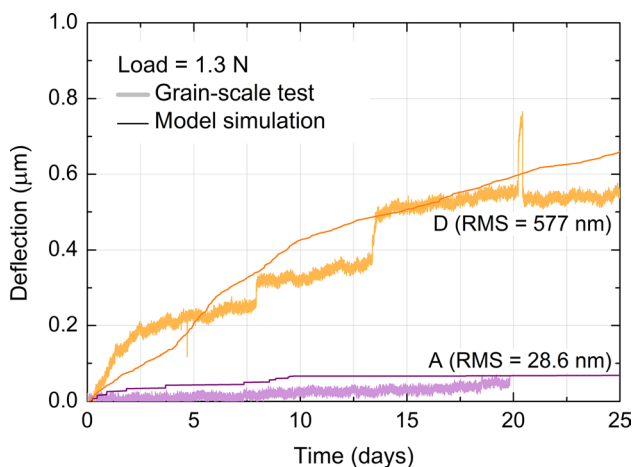
Fig. 14 Simulated Tests A and D with the calibrated model (color figure online)

6 Final remarks

A model was devised to simulate the response of sand grains to sustained loads. Deflection of a loaded grain has two distinct time-dependent components: displacement caused by creep of the core mineral in the grain and the displacement owed to static fatigue of the rough surfaces at the contacts with loading platens. The two are calculated separately as their scales differ and require different model resolutions. The tool used to construct the model is the distinct element method, with both the grain and the contact region simulated separately by assemblies of spherical sub-particles with bonds subjected to complex loads and to the stress corrosion process.

The model was calibrated using existing results from physical tests on silica grains with surfaces of different roughness. The calibrated model is applicable to grains loaded with forces characteristic of weak to medium-strong force chains in shallow sand deposits. The model was not constructed to predict grain splitting or crushing; rather, it was developed to mimic the time-dependent response of individual grains to sustained loads, with attention paid to the process at the rough contacts. Time-dependent response of grains to sustained loads is a building block in the response of sand deposits to long-term loads. The latter has important engineering consequences in freshly deposited or disturbed sand. One of those consequences is an increase in small-strain stiffness of sand at the macroscopic scale, *e.g.* [1]. There are reasons to believe that the macroscopic stiffness at larger strains also increases as a result of sustained loading, but changes in strength are not as distinct [9]. The evolution of the sand stiffness is part of the sand ageing process, and contact maturing (Michalowski et al. [27]) may prove to be the dominant phenomenon contributing to this process.

The evolution of the rough grain contact region, as seen in simulations (Fig. 11), is consistent with the static fatigue hypothesis [26], where the delayed fracturing of simulated contact asperities was thought to lead to an increase in the number of contact points within the nominal contact area. Consequently, the load transferred through the contact becomes progressively more uniformly distributed over the nominal contact area as the process continues (Fig. 12). This, in turn, produces an increase in the stiffness of the contacts, and results in an increase of the macroscopic stiffness of sand. The model predicts the decaying intensity of grain deflection under a sustained load.

The contact process appears to be captured well by the model. Calibrated with the laboratory tests, the model reproduces the deflection of grains to prolonged loads. The chief tool in constructing the model is the distinct element

approach. As the surface topography of many geomaterials, including silica sand, has a self-affine (fractal) characteristic, reproducing the contact geometry is a challenge for the distinct element method. The simulations indicated, however, that it is a promising tool, and even with a limited resolution, a reasonable outcome is obtained. Future research will include interaction between grains, development of a contact constitutive law, and extending the approach to networks of force chains in sand.

Compliance with ethical standards

Conflict of interest The authors declare that they have no conflict of interest.

References

1. Afifi, S.S., Woods, R.D.: Long-term pressure effects on shear modulus of soils. J. Soil Mech. Found. Div. **97**(10), 1445–1460 (1971)
2. Archard, J.: Elastic deformation and the laws of friction. Proc. Roy. Soc. A.-Math. Phy. **243**(1233), 190–205 (1957)
3. Barber, J.R.: Contact mechanics, vol. 250. Springer, Berlin (2018)
4. Bažant, Z.P.: Size effect on structural strength: a review. Arch. Appl. Mech. **69**(9–10), 703–725 (1999)
5. Brzesowsky, R., Hangx, S., Brantut, N., Spiers, C.: Compaction creep of sands due to time-dependent grain failure: effects of chemical environment, applied stress, and grain size. J. Geophys. Res.-Sol. EA. **119**(10), 7521–7541 (2014)
6. Cavarretta, I., Coop, M., O'Sullivan, C.: The influence of particle characteristics on the behaviour of coarse grained soils. Géotechnique **60**(6), 413–423 (2010)
7. Cil, M., Alshibli, K.: 3D evolution of sand fracture under 1D compression. Géotechnique **64**(5), 351 (2014)
8. Cole, D.M., Peters, J.F.: Grain-scale mechanics of geologic materials and lunar simulants under normal loading. Granul. Matter **10**(3), 171–185 (2008)
9. Daramola, O.: Effect of consolidation age on stiffness of sand. Géotechnique **30**(2), 213–216 (1980)
10. Einav, I.: Breakage mechanics—part I: theory. J. Mech. Phys. Solids **55**(6), 1274–1297 (2007)
11. Greenwood, J.A., Williamson, J.P.: Contact of nominally flat surfaces. Proc. Roy. Soc. A.-Math. Phy. **295**(1442), 300–319 (1966)
12. Greenwood, J.A., Tripp, J.H.: The elastic contact of rough spheres. J Applied Mechanics **34**(1), 153–159 (1967)
13. Hanaor, D.A., Gan, Y., Einav, I.: Contact mechanics of fractal surfaces by spline assisted discretisation. Int. J. Solids Struct. **59**, 121–131 (2015)
14. Hertz, H.: Ueber die Beruhrung fester elastischer Korper. J. Reine. Angew. Math. **92**, 156–171 (1882)
15. Hiramatsu, Y., Oka, Y.: Determination of the tensile strength of rock by a compression test of an irregular test piece. Int. J. Rock. Mech. Min. Sci, **3**(2), 89–90 (1966)
16. Hiramatsu, Y., Oka, Y.: Determination of the tensile strength of rock by a compression test of an irregular test piece: authors' reply to discussion Int. J. Rock. Mech. Min. Sci. **4**(3), 363–365 (1967)
17. Hyun, S., Pei, L., Molinari, J.-F., Robbins, M.O.: Finite-element analysis of contact between elastic self-affine surfaces. Phys. Rev. E **70**(2), 026117 (2004)
18. Jacobs, T.D., Junge, T., Pastewka, L.: Quantitative characterization of surface topography using spectral analysis. Surf. Topogr. **5**(1), 013001 (2017)
19. Jerier, J., Molinari, J.: Normal contact between rough surfaces by the discrete element method. Tribol. Int. **47**, 1–8 (2012)
20. Kanafi, M.M., Tuononen, A.J.: Top topography surface roughness power spectrum for pavement friction evaluation. Tribol. Int. **107**, 240–249 (2017)
21. Lade, P.V., Karimpour, H.: Static fatigue controls particle crushing and time effects in granular materials. Soils Found. **50**(5), 573–583 (2010)
22. Li, Q., Tullis, T.E., Goldsby, D., Carpick, R.W.: Frictional ageing from interfacial bonding and the origins of rate and state friction. Nature **480**(7376), 233–236 (2011)
23. Mandelbrot, B.B.: The fractal geometry of nature. WH Freeman, New York (1983)
24. McDowell, G., Harireche, O.: Discrete element modelling of soil particle fracture. Géotechnique **52**(2), 131–135 (2002)
25. Mesri, G., Feng, T., Benak, J.: Postdensification penetration resistance of clean sands. J. Geotech. Eng.-ASCE **116**(7), 1095–1115 (1990)
26. Michalowski, R.L., Nadukuru, S.S.: Static fatigue, time effects, and delayed increase in penetration resistance after dynamic compaction of sands. J. Geotech. Geoenviron. Eng. **138**(5), 564–574 (2012)
27. Michalowski, R.L., Wang, Z., Nadukuru, S.S.: Maturing of contacts and ageing of silica sand. Géotechnique **68**(2), 133–145 (2018)
28. Michalowski, R.L., Wang, Z., Nadukuru, S.S., Mesri, G., Kane, T.: Maturing of contacts and ageing of silica sand—discussion. Géotechnique **69**(8), 748–749 (2019)
29. Mitchell, J.K., Solymar, Z.V.: Time-dependent strength gain in freshly deposited or densified sand. J. Geotech. Eng.-ASCE **110**(11), 1559–1576 (1984)
30. Mitchell, J.K.: Aging of sand–a continuing Enigma? In: 6th International Conference on Case Histories in Geotechnical Engineering. Arlington, VA (2008)
31. Nakata, Y., Kato, Y., Hyodo, M., Hyde, A.F., Murata, H.: One-dimensional compression behaviour of uniformly graded sand related to single particle crushing strength. Soils. Found. **41**(2), 39–51 (2001)
32. Orford, J., Whalley, W.: The quantitative description of highly irregular sedimentary particles: the use of the fractal dimension. In: Marshall, J.R. (ed.) Clastic Particles, pp. 267–280. Van Nostrand Reinhold, New York (1987)
33. Pei, L., Hyun, S., Molinari, J., Robbins, M.O.: Finite element modeling of elasto-plastic contact between rough surfaces. J. Mech. Phys. Solids **53**(11), 2385–2409 (2005)
34. Pejchal, V., Žagar, G., Charvet, R., Dénéréaz, C., Mortensen, A.: Compression testing spherical particles for strength: theory of the meridian crack test and implementation for microscopic fused quartz. J. Mech. Phys. Solids **99**, 70–92 (2017)
35. Persson, B., Albohr, O., Tartaglino, U., Volokitin, A., Tosatti, E.: On the nature of surface roughness with application to contact mechanics, sealing, rubber friction and adhesion. J. Phys.-Condens. Mat. **17**(1), R1–R62 (2005)
36. Pohrt, R., Popov, V.L.: Normal contact stiffness of elastic solids with fractal rough surfaces. Phys. Rev. Lett. **108**(10), 104301 (2012)

37. Potyondy, D.O., Cundall, P.: A bonded-particle model for rock. Int. J. Rock Mech. Min. Sci. **41**(8), 1329–1364 (2004)

38. Potyondy, D.O.: Simulating stress corrosion with a bonded-particle model for rock. Int. J. Rock Mech. Min. Sci. **44**(5), 677–691 (2007)

39. Robertson, D., Bolton, M.: DEM simulations of crushable grains and soils. In: Powders and Grains: Fourth International Conference on Micromechanics of Granular Media. Sendai, Japan: CRC Press (2001)

40. Schmertmann, J.H.: The mechanical aging of soils. J. Geotech. Eng.-ASCE **117**(9), 1288–1330 (1991)

41. Scholz, C.: Mechanism of creep in brittle rock. J. Geophys. Res. **73**(10), 3295–3302 (1968)

42. Scholz, C.H.: Static fatigue of quartz. J. Geophys. Res. **77**(11), 2104–2114 (1972)

43. Senetakis, K., Coop, M.R., Todisco, M.: Tangential load–deflection behaviour at the contacts of soil particles. Geotech. Lett. **3**(2), 59–66 (2013)

44. Vallejo, L.E.: Fractal analysis of granular materials. Géotechnique **45**(1), 159–163 (1995)

45. Wang, Z., Michalowski, R.L.: Contact fatigue in silica sand—Observations and modeling. Geomech. Energy. Envir. **4**, 88–99 (2015)

46. Wang, Z., Michalowski, R.L.: An Apparatus for Testing Static Fatigue at Sand Grain Contacts. Geotech. Test. J. **41**(3), 448–458 (2018)

47. Wei, D., Zhao, B., Dias-da-Costa, D., Gan, Y.: An FDEM study of particle breakage under rotational point loading. Eng. Fract. Mech. **212**, 221–237 (2019)

48. Yang, H., Baudet, B.A., Yao, T.: Characterization of the surface roughness of sand particles using an advanced fractal approach. Proc. Roy. Soc. A.-Math. Phy. **472**(2194), 20160524 (2016)

49. Zhai, C., Hanaor, D., Gan, Y.: Contact stiffness of multiscale surfaces by truncation analysis. Int. J. Mech. Sci. **131**, 305–316 (2017)